sustainability

MDPI

Article

Sustainable Approach of Mineral Dispersion Recovery from the Technological Wastewater Resulting from Porcelain Manufacturing

Simona Elena Avram [1], Lucian Barbu Tudoran [2,3], Gheorghe Borodi [3], Miuta Rafila Filip [4], Raluca Anca Mereu [5] and Ioan Petean [5,*]

[1] Faculty of Materials and Environmental Engineering, Technical University of Cluj-Napoca, 103-105 Muncii Bd., 400641 Cluj-Napoca, Romania; simona.avram@imadd.utcluj.ro
[2] Faculty of Biology and Geology, Babes-Bolyai University, 44 Gheorghe Bilaşcu Street, 400015 Cluj-Napoca, Romania; lucian.barbu@ubbcluj.ro
[3] National Institute for Research and Development of Isotopic and Molecular Technologies, 65-103 Donath Street, 400293 Cluj-Napoca, Romania; borodi@itim-cj.ro
[4] Raluca Ripan Institute for Research in Chemistry, Babeș-Bolyai University, 30 Fantanele Street, 400294 Cluj-Napoca, Romania; miuta.filip@ubbcluj.ro
[5] Faculty of Chemistry and Chemical Engineering, Babes-Bolyai University, 11 Arany Janos Street, 400028 Cluj-Napoca, Romania; raluca.mereu@ubbcluj.ro
* Correspondence: ioan.petean@ubbcluj.ro

Abstract

Porcelain manufacturing technological wastewater contains many mineral particles, like kaolinite 27%, quartz 29%, calcium feldspar 15%, and mullite 12%. These particulate matters are dispersed into the wastewater from all technological steps influencing the water parameters, such as pH, electrical conductivity, total dissolved solids (TDS) and turbidity. These properties were measured and correlated with the physicochemical investigation of the collected particles. The two sample types are as follows: particles collected directly from the wastewater dispersion (WWS) and the slurry (SLR) collected from the dump. The mineral distribution was assessed by XRD correlated with mineralogical optical microscopy, revealing the relative distribution of the finest kaolinite particles with respect to quartz and feldspar boulder-like particles. Mullite was observed as a rounded inclusion occurring due to the re-circulated grounded material. It results in the presence of sodium silicate, acting as a densification binder when the samples are completely dried. Particle morphology was correlated with their elemental composition through SEM–EDX investigation. Iron hydroxide was found at about 9%. It prevents re-circulation of this wastewater slurry in porcelain production. Thus, a sustainable approach is required for its utilization as a sub-product. Therefore, the samples were subjected to thermal analysis in order to reveal its sintering behavior. Thermal analysis revealed the dehydroxylation of kaolinite between 530 and 630 °C, and a high-temperature thermal event at 994 °C (WWS) and 997 °C (SLR), which was further confirmed by DSC and attributed to mullite formation. Particle consolidation through the dehydroxylated kaolinite matrix and further mullitized mass was assessed through SEM microscopy, indicating proper densification to ensure slurry utilization for less pretentious ceramic products, allowing them to be fired at relatively lower temperature than porcelain (e.g., 600–800 °C) and ensuring a significant energy consumption saving.

Keywords: porcelain wastewater; particle distribution; sustainable recycling; kaolinite dehydroxylation; ceramic sludge

Check for updates

Academic Editor: Antonio Caggiano

Received: 31 July 2026
Revised: 14 August 2026
Accepted: 17 August 2026
Published: 18 August 2026

Copyright: © 2026 by the authors. Licensee MDPI, Basel, Switzerland. This article is an open access article distributed under the terms and conditions of the Creative Commons Attribution (CC BY) license.

1. Introduction

Porcelain itself has been renowned since ancient times, representing a hallmark of quality and refinement characteristic of China [1,2]. Admiration for these exceptional works of art has spurred the development of this field worldwide, starting with the 18th century [3,4]. The production of porcelain goods constitutes a significant part of the ceramics sector. It is renowned for fine, high-quality products that frequently feature elaborate ornamentation, positioning them as works of art and luxury items. Global statistics indicate steady growth in this sector over the past decade, peaking between 2021 and 2022, followed by a moderate decline driven by changes in the Chinese real estate market [5,6]. The specific production is dominated by China, followed by India, Vietnam and Brazil, having fine artwork components as well as porcelain tiles and sanitaryware [6]. On the other hand, the production size is about 14 to 15 billion square meters of products.

Sustainability shapes the general trend within the porcelain industry, implying three main directions: the first is decarbonization through the use of environmentally friendly energy, the second direction is recycling of the wastes through the circular economy and the third direction is natural resource conservation (e.g., protection of main raw material deposits like kaolinite, feldspar and silica) [7,8]. Indeed, the use of electricity generated from eco-friendly sources, such as hydrogen, hydroelectric, wind, or solar power, leads to significant decarbonization of production within the sector [9,10]. On the other hand, some of the direct wastes, like porcelain dust, resulting from the polishing procedures can be recycled directly into the process as an additive to the raw material by preserving its composition and purity through the working process, but it is effective in geopolymers or other ceramic composition with red clays due to its fine pozzolanic action and status as a microstructural enhancer [11–13]. Such an approach ensures a good decarbonization of the building materials sector by reducing the consumption of Portland cement. Production scrap is ground down and reintroduced into the production flow as raw material; consequently, from this perspective, the principles of the circular economy are upheld.

There is another category of ceramic waste resulting from porcelain production: the sludge obtained from filtering industrial wastewater. This type of powdery waste originates from all stages of the production process, starting with raw material preparation and ending with the final grinding following the firing of the porcelain products. In addition to various ceramic particles generated during the processing stages, the waste also contains oxide material detached from the mechanical components of the production line. Thus, its contamination with iron oxides and hydroxides—resulting from contact with rusted parts along the production line—is known in the literature to render its recirculation into the primary production process impossible, as observed in our previous studies regarding the slurry collected from ceramic tile wastewater [14,15]. Our observations indicate that an iron hydroxide content of approximately 8–9% adversely affects the slurry collected from industrial wastewater generated during the production of floor and wall tiles. These studies highlighted the tendency of iron hydroxides to contaminate the kaolinite matrix. While slurry from porcelain production wastewater is expected to exhibit similar behavior, notable differences may arise; consequently, advanced physicochemical investigations are required, consisting of a novel sustainable approach. The causes are not related to the microstructure or the cohesion of the ceramic material, but rather to the staining of the outer glaze with brown hues; this results in unsightly rejects [16,17], a particularly troublesome issue for refined porcelain art pieces. For instance, Barrachina et al. observe that iron hydroxides found in the kaolinite raw material should be below 1% and overall content during the ball milling process should not exceed 3% because it will generate brown hues [18]. This fact is confirmed by other research [19,20].

These solid particles are extracted from industrial wastewater via pressing, resulting in a pasty sludge that is deposited in a wet-method tailings pond. Its drying weakens the cohesion between particles, leading to the release into the atmosphere of a multitude of fine, powdery fractions including kaolinite, quartz, and other associated minerals [21]. Quartz particles are predominantly found in the PM10 range, whereas clay particles such as kaolinite generate fractions primarily in the PM1 and PM2.5 ranges [21]. Consequently, pollution involving such particulate emissions can lead to silicosis [22], bronchial asthma [23–25], and even lung cancer [26,27].

Consequently, it is necessary to keep this powdery waste in a permanently moist state, a requirement that not only takes up space but also consumes resources, rendering its long-term management unsustainable. Thus, it is essential to identify specific applications where this ceramic-based sludge can be utilized as a raw material for a by-product.

Advanced microstructural investigations applied to these powdery wastes are essential for evaluating their valorization potential. The distribution of constituent minerals can be elucidated in detail by combining X-ray diffraction with mineralogical microscopy under cross-polarized light [28,29]. Precision regarding microstructural details is ensured by scanning electron microscopy (SEM), which offers the advantage of EDX elemental analysis [30,31]. The results of these analyses, correlated with the properties of the industrial wastewater generated during porcelain production, will enable a comprehensive microstructural characterization. However, this alone is insufficient, as the thermal behavior must be evaluated to precisely determine critical temperatures, such as those for the dehydroxylation of clayey materials and their subsequent mullitization. Consequently, DSC analysis coupled with DTG is required [32,33]. Changes in the structural chemical bonds of the sludge in question—specifically the loss of OH bonds—can be identified using FTIR spectroscopy [34]. The aim of this research is to determine an optimal composition for ceramic sludge recovered from industrial wastewater generated during porcelain production, as well as to establish future directions for its valorization as a by-product.

2. Materials and Methods

2.1. Sampling Protocol

The used water samples and the ceramic slurry resulting from the pressing filtration process were collected from the technological flux (Figure 1) of a porcelain manufacturing facility in Cluj County Romania (the production facility name is kept anonymous due to economic reasons). It is a factory with a medium-scale production line focused on manufacturing mugs, cups, and saucers for the hospitality industry. Production volume ranges from 1 to 3 tons per month, depending on current orders.

The technological process employed utilizes a moldable kaolinite slip with a water consumption of approximately 45 L per 100 kg of dry mass. The granular raw material consists of 55% kaolinite, 25% quartz, and 20% feldspar. The specific type of feldspar used is not specified and remains to be identified through physicochemical analyses. Sodium silicate is used as an anti-flocculating agent at a level of approximately 400 g (the exact percentage is considered classified as a proprietary production detail) per 100 kg of dry raw material powder.

The volume of the used process water ranges from 3 to 5 cubic meters per month, depending on current production. It is collected in a sedimentation tank where coarse particles settle at the bottom, while ultra-fine particles remain suspended in the water.

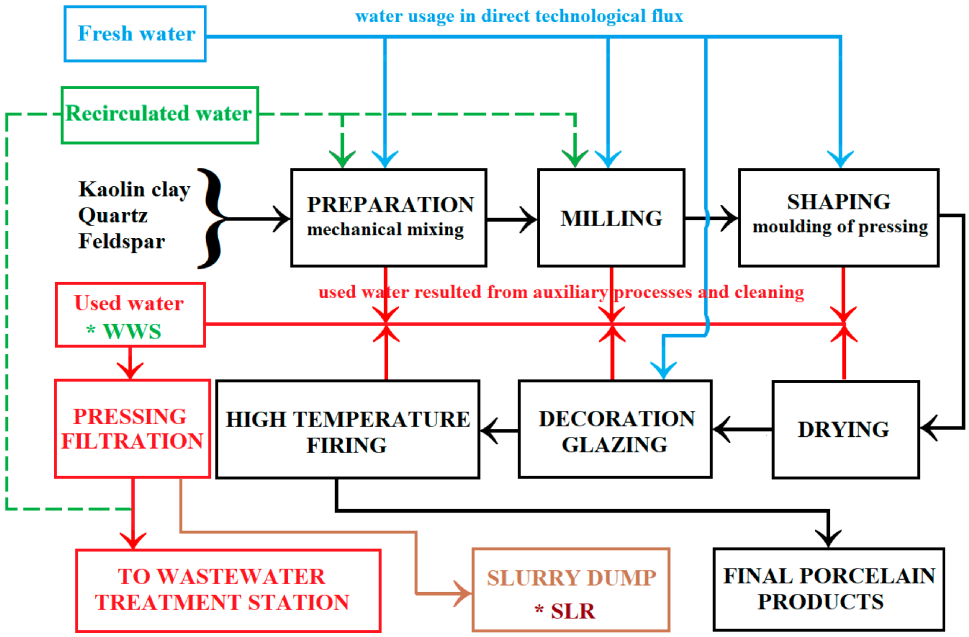


Figure 1. Porcelain manufacturing working flow with description of the water circuit. (WWS—wastewater sediment; SLR—slurry collected from the dumpsite; their sampling point on the working flow is marked with *).

The used technological water samples (WW) were collected from the storage tank from three different levels: from the top, from the middle of the tank (1 m depth) and from the layer immediately above the bottom sediments (1.75 m depth) to ensure a good statistical relevance of their physicochemical properties. The mean values were obtained as the arithmetic average of three measurements on each sample. Samples of 2.5 L each were collected, stored in new bottles, and taken to the laboratory. The same physicochemical properties were measured for the filtered water (FW); their mean values were calculated as an arithmetic average of at least three distinct measurements. Afterward, the sediment gathered on the bottom of the bottles was collected and mixed onto a representative sediment sample (WWS) which was further subjected to complex analysis.

Manufacturer procedures periodically collect the sediment from the bottom of the wastewater tank and dump it along with the slurry resulting after the pressing filtration to the slurry bunker. The bunker is emptied once a year when the producer delivers this waste to a specialized landfill, a process that increases production costs. Slurry dumps collect the pressed mud resulting from different porcelain charges, which might involve some compositional variations and might affect the overall behavior of the measurements. Therefore, equal quantities of slurry were collected from three different spots from the surface of the dump bunker and three samples from a depth of 1 m. Equal quantities of 100 g from each collected sample were mixed into an average representative sample (SLR).

2.2. Investigation Methods

Water physicochemical properties like pH, electrical conductivity, total dissolved solids and salinity were measured using a multi-parameter device HANNA HI 9829, produced by Hanna Instruments Co., Bedfordshire, UK. There were at least three measurements for each sample. The mean values were statistically analyzed with Anova test followed by Tukey post hoc analysis at a significance level of $\alpha = 0.05$ using Origin software version 2019b (Microcal Company, Northampton, MA, USA).

X-ray diffraction (XRD) analysis was performed using a Bruker D8 Advance diffractometer (Bruker Company, Karlsruhe, Germany) in Bragg–Brentano configuration,

equipped with a copper anticathode and using monochromatic radiation Cu kα radiation (1.540562 Å). The diffraction regime is: 2θ range from 5 to 80° at a speed of 1°/min, voltage 40 kV, current 40 mA, step size of 0.02° and count per step of 0.5 s. Diffraction peaks were identified using Match 1.0 software, utilizing the PDF2 database from Crystal Impact Company (Crystal impact Company, Bonn, Germany).

Samples for optical microscopy were prepared using the smear method. Specifically, a few drops of WWS were placed and spread onto a glass slide and allowed to air-dry. The SLR slurry sample was smeared onto the surface of a glass slide and left to air-dry. Once dried, the slides were subjected to mineralogical microscopic analysis. It was effectuated under cross polarized light observation with a Laboval 2 microscope produced by Zeiss Company (Oberkochen, Germany). Two magnification ranges were used at ×300 (sale bar of 200 μm) and ×1200 (scale bar of 50 μm). Digital image acquisition was carried out using a Sony 14 MPx digital photo camera (Sony company, Minato, Japan).

Scanning Electron Microscopy (SEM) was performed using a Hitachi SU8230 microscope (Hitachi Company, Tokyo, Japan) operated in high-vacuum mode at an accelerating voltage of 30 kV at a working distance of 15 mm to ensure an optimal quantification of light and heavy elements that might occur in the sample's composition. The samples were metalized with a thin layer of gold to ensure optimal electrical conduction; the Au component was subtracted during the elemental analysis. Secondary Electron Images (SEIs) were taken for advanced microstructural observation. Elemental investigations were effectuated with Aztec X-Mas 1160 EDX detection module (Oxford Instruments, Oxford, UK) ensuring optimal recording of Backscattered electron Images (BSEs) with elemental distribution map and Energy Dispersive Spectroscopy (EDS).

Particle size distribution was effectuated on SEM images using Image J software version 1.53k (National Institute of Health, Bethesda, MD, USA) using cell counter plugin and a threshold range from 0 to 100 μm with progressive steps of 5 μm. The chart output was represented in Origin software version 6.0 (Microcal Company, Northampton, MA, USA).

The simultaneous thermal analysis was done with SDTQ600 TA Instruments (TA Instruments, New Castle, DE, USA) recording TG, DTA and DSC curves. Approximate 10 mg of sample was heated from 25 to 1400 °C with a speed of 10 °C/min in dynamic air flow.

Fourier Transformed Infrared Spectroscopy (FTIR) was done with a JASCO 610 spectrophotometer (JASCO International Co., Ltd., Tokyo, Japan) directly on the powder samples using the Attenuated Reflectance mode (ATR) in the range of 500–4000 cm^{-1} with a resolution of 4 cm^{-1} and 100 scans for each spectrum.

Atomic Force Microscopy (AFM) has been effectuated using a Jeol JSPM 4210 scanning probe microscope (Jeol Company, Tokyo, Japan) operated in tapping mode with silicon nitride tip NSC15-Hard produced by Mikromasch (Sofia, Bulagria) having a resonant frequency of 330 kHz and a force constant of 40 N/m. The topographic images were analyzed with WinSPM software version 2.0 (Jeol Company, Tokyo, Japan).

3. Results

3.1. Wastewater Properties

The filtering process plays the key role of the removal of mineral particulate matter from the technological wastewater and subsequently the physicochemical parameters must be monitored (Table 1). Their representation with statistical markers is displayed in Figure 2.

Table 1. Water physicochemical properties.

Samples	pH	Electrical Conductivity, µS/cm	TDS, mg/L	Salinity, PSU	Turbidity, FTU
WW	10.27	1489	743	0.77	93.67
	10.14	1512	752	0.84	94.12
	10.59	1506	732	0.68	93.44
Mean value	**10.33**	**1502.33**	**742.33**	**0.76**	**93.74**
SD±	**0.18**	**9.74**	**8.17**	**0.06**	**0.28**
FW	9.54	1115	607	0.63	2.99
	9.63	1148	612	0.68	3.19
	9.41	1069	594	0.59	3.07
Mean value	**9.52**	**1110.66**	**604.33**	**0.63**	**3.08**
SD±	**0.09**	**32.39**	**7.58**	**0.03**	**0.08**

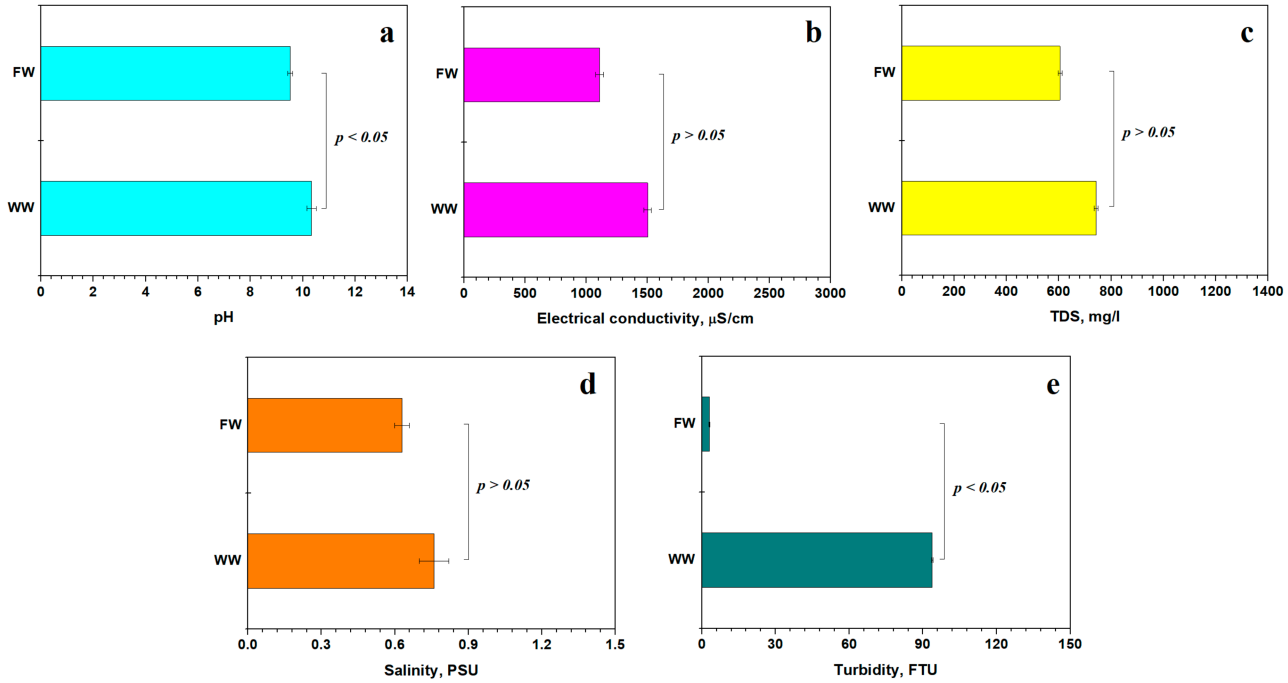


Figure 2. Water sample physicochemical properties: (**a**) pH, (**b**) electrical conductivity, (**c**) total dissolved solids (TDS), (**d**) salinity and (**e**) turbidity.

The interaction of material particles upon their dispersion in water depends strictly on their solubility. Consequently, particles of a siliceous nature such as quartz and clays are insoluble, while sedimentary carbonaceous rocks have moderate solubility (e.g., calcite has a solubility of 13 mg/L [35]) and the iron hydroxides are practically insoluble but their structure is sensitive to water, which constitutes the difference between lepidocrocite and goethite [36,37].

The presence of silicon might retard the goethite nucleation during the lepidocrocite transformation into goethite, but it is ineffective if the germination seeds are already formed [37]. This fact has great importance regarding the distribution of iron hydroxides within the wastewater particulate matter.

Consequently, we observe that turbidity and pH show statistically significant differences ($p < 0.05$) because of the filtration process. The high turbidity of the used process water sample indicates the presence of numerous dispersed solid particles that are removed

through filtration. Furthermore, given the involvement of porcelain, the water contains many fine kaolinite particles, which certainly influences the pH value. The natural aqueous dispersion of fine kaolinite particles typically exhibits an alkaline pH due to OH^- ions, but in acid conditions (pH range 4–6) the octahedral faces interacting with water facilitate particle clustering [38]. However, the acidic conditions lead to the particles clustering, and the deflocculant agent (like sodium silicate) adjusts pH values to an alkaline range in order to maintain the fine suspended kaolinite particles [39]. The remnant moisture within the pressed sludge retains small quantities of deflocculant agent within the kaolinite particles, explaining the significant decrease in pH observed in Figure 2a.

Dissolved solids facilitate the electrical conductivity of the water and increase its salinity, as observed in Figure 2b–d. A slight decrease in these values is observed after filtration, though it is not statistically significant. In practice, dissolved solids are almost entirely removed via the filtrate, with only a small residual amount remaining in the moisture of the sludge produced after pressing. For example, it would be the case of sodium silicate or ethyl silicate, known as soluble glass, which is used as a deflocculant agent to ensure optimal dispersion of the particles and subsequently their binding in the raw pressed ceramic parts [40,41]. Consequently, a small amount of soluble glass will remain adsorbed on the surface of the mineral particles after the sludge is pressed.

3.2. Mineral Composition

XRD reveals (Figure 3) that both sediments collected from the technological wastewater (WWS) and slurry collected from the dump (SLR) have pronounced crystalline structure. It is characterized by predominantly intense and narrow peaks followed by several less intense and broadened peaks belonging to refined particulate matter.

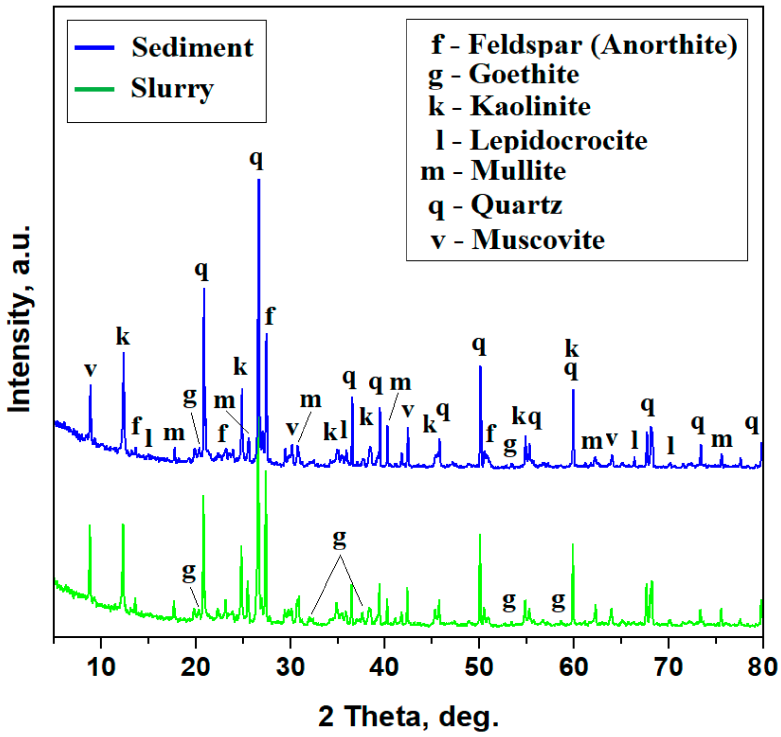


Figure 3. XRD patterns resulted for the investigated samples.

Both patterns are dominated by quartz peaks, which are very intense and narrow, corresponding to highly crystalline particles that should have a dense and compact microstructure of boulder-like particles, such as the green grey ones in Figure 4a. The following intensity suite is given by kaolinite peaks, especially the one at 12.39°, which is narrow

and well developed, indicating a relatively high content within the samples. However, some other kaolinite peaks, like the one at 45.16°, are significantly broadened, indicating the presence of very small particles and giving the white shallow observed in Figure 4c, which becomes denser in Figure 4d as a consequence of pressing (a better view of these aspects requires an advanced microstructural investigation under high magnification by SEM microscopy). Another intense suite of peaks belongs to feldspar, which proves to be calcium feldspar crystallized as anorthite, having bright white particles, clearly observable in Figure 4. It is well known in the literature for its use in special porcelains, like those for dental applications [42], unlike potash feldspar, which is commonly used for high-translucence porcelain [43,44].

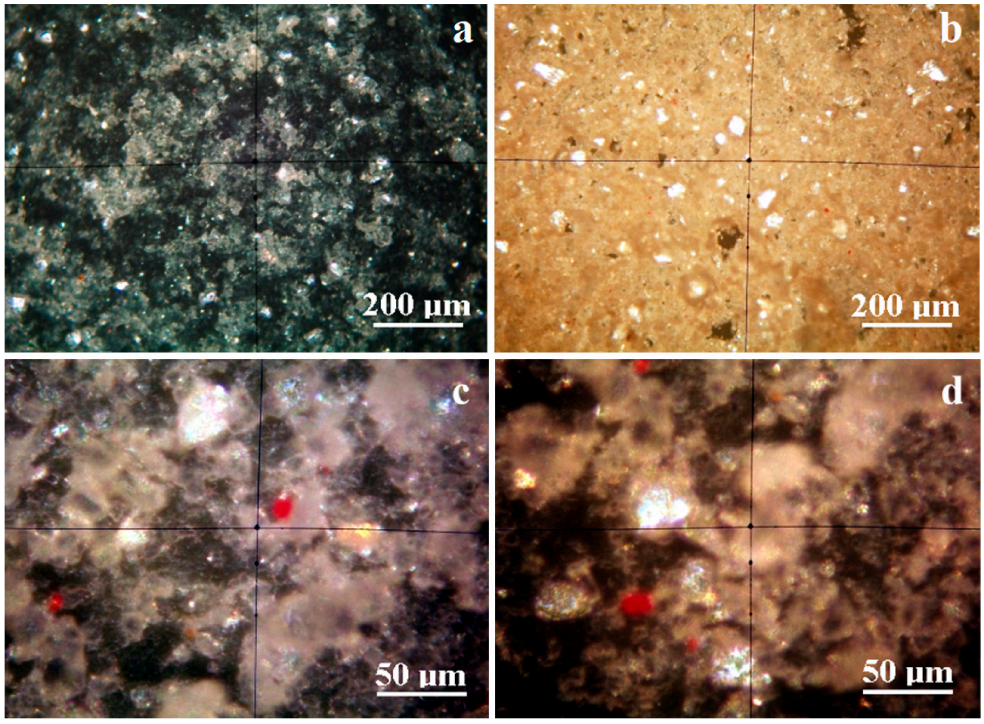


Figure 4. Cross-polarized light microscopy (crossed nicols) images of the investigated samples at low magnification ×300 (sale bar of 200 µm): (**a**) WWS and (**b**) SLR and at high magnification ×1200 (scale bar of 50 µm): (**c**) WWS and (**d**) SLR.

The presence of muscovite is confirmed by well-developed, albeit less intense, diffraction peaks, consistent with the sparse occurrence of pink lamellar particles dispersed within the kaolinite matrix (Figure 4c,d). Mullite particles are found both in SWS and SLR as small boulder particles with intense red color. The presence of iron hydroxide is evidenced by specific diffraction peaks which are less intense and broadened because of their small particles size but also by the mixing with the kaolinite matrix, which makes them difficult to observe, but their presence gives a brown tarnish to the kaolinite matrix in the slurry resulting after pressing filtration (Figure 4b). It is very interesting that lepidocrocite seems to predominate in the sediment sample corresponding to the most degraded form of iron hydroxides, while the pressed slurry better evidences goethite peaks, demonstrating appreciable lepidocrocite content, a fact in good agreement with the literature and revealing their transformation with respect to long-lasting moisture content [36,37].

The presence of a deflocculant agent is evidenced by the greenish shade next to the mineral particles in Figure 4a, which is caused by the sodium silicate soluble glass. These are small remains attached to the particles, while most sodium silicate remains in the filtered water sample. Thus, the XRD pattern does not reveal relevant peaks for it; as a

consequence, it is fair to consider that its amount falls below the detection limit. The dense pressed particles in Figure 4b did not allow us to observe the traces of sodium silicate.

The Relative Intensity Ratio (RIR) method allows the calculation of the exact percent of each mineral within the XRD pattern of the sample, taking into consideration the intensities of each mineral's diffraction peaks without overlapping with other minerals (the most representative individual peak for each mineral is mentioned in Table 2) and their corundum factor [14,45].

Table 2. XRD-RIR results and correlation with cross-polarized light microscopy.

Component	Quartz	Kaolinite	Muscovite	Mullite	Anorthite	Iron Hydroxides
Formula	SiO_2	$Al_2Si_2O_5(OH)_4$	$KAl_2(AlSi_3O_{10})(F,OH)_2$	$Al_6Si_2O_{13}$	$CaAl_2Si_2O_8$	FeO(OH)
Color nuances	Green-gray	White-blue	Pink	Intense red	Bight white	Reddish-brown
Representative peak, 2θ°	26.68	12.48	8.96	40.89	27.90	35.73
Sediment—WWS						
Amount, wt.%	32	24	9	11	17	7
Particle size, μm	5–50	1–20	1–35	2.5–15	3–50	2–5
Slurry—SLR						
Amount, wt.%	29	27	8	12	15	9
Particle size, μm	5–60	1–25	1–40	2.5–20	3–55	2.5–5

Note: RIR being a semi-quantitative method, an associated uncertainty of ±3–5% should be considered.

The results obtained are presented in Table 2. They reveal the predominance of quartz followed closely by clay particles (e.g., mostly kaolinite with traces of muscovite) and anorthite feldspar took third place. The amount of mullite is significantly low, and iron hydroxides are situated lower but still enough to disturb the possibility of slurry recirculation in the same technological process.

Cross-polarized light microscopy images in Figure 4 allow the proper measurement of the particle size range, revealing that quartz and anorthite feldspar consist of coarse particles ranging from about 5 to 50 μm, while mullite particles are slightly finer, at about 2.5–15 μm. They have two sources. They primarily originate in the firing process and subsequent polishing of the products, while the secondary source is re-circulated porcelain scraps, which were milled and re-introduced in the raw material. XRD correlated with cross-polarized light observation evidence indicating their presence, but it cannot distinguish their source. Clay particles are predominantly fine within the range of 1–10 μm. Only some sparse lamellas have planar size of 20–35 μm.

Overall, it can be observed that sediment collected directly from the water has significantly increased amounts of quartz and feldspar compared to that in the pressed slurry; the difference is explained by the finest fractions of kaolinite, which remain suspended for a long time because of the alkaline pH induced by the deflocculant agent. Therefore, the amount of kaolinite increases after the pressing process because filtration enables a more effective removal of fine particles from the wastewater. The small differences might involve some more consistent implication regarding the microstructural aspect.

3.3. Microstructural Aspects and Elemental Composition

Secondary Electron Images (SEIs) can capture complex microstructural features, both at the level of the material's overall structure (e.g., low magnification) and regarding fine microstructural details (e.g., high magnification). We acquired the BSE images at the

exact same location and magnification as the SEI images and superimposed the elemental distribution map onto them. The EDS spectrum was recorded over the entire area of the BSE image to determine the elemental composition. This was expressed in atomic percentages to better correlate with the stoichiometry of the minerals identified in the samples.

The detected elements were labeled with specific colors, including: O—turquoise, Si—green, Al—yellow, K—red, Ca—Blue and Fe—orange. Thus, quartz particles have an intense green color, clay particles are pale green for kaolinite, while muscovite has extra red spots due to the presence of K. Anorthite feldspar has an optimal identification marker following the distribution of Ca atoms, evidenced by blue spots. Iron hydroxides in both forms, lepidocrocite and goethite, appear as orange spots and subsequently orange areas where their contamination spreads through the finest particle matrix.

The overall microstructural aspects of the WWS sample (Figure 5a) reveal the coarse granular matter of 3–50 µm formed by quartz and feldspar particles tightly surrounded by a dense matrix of fine kaolinite particles. The orange spots spread within the kaolinite matrix represent the distribution of iron hydroxides, proving the contamination of the kaolinite matrix. The bigger fractions having a dense and compact internal structure are resistant to the penetration of small iron hydroxides. This observation is sustained by the elemental composition within the EDS spectrum where O and Si are dominant elements followed by Al, indicating the prevalence of kaolinite after quartz, while the presence of K is related to the presence of muscovite. Anorthite particles are well represented by 0.6 at.% Ca and iron hydroxides by 0.2 at.% Fe.

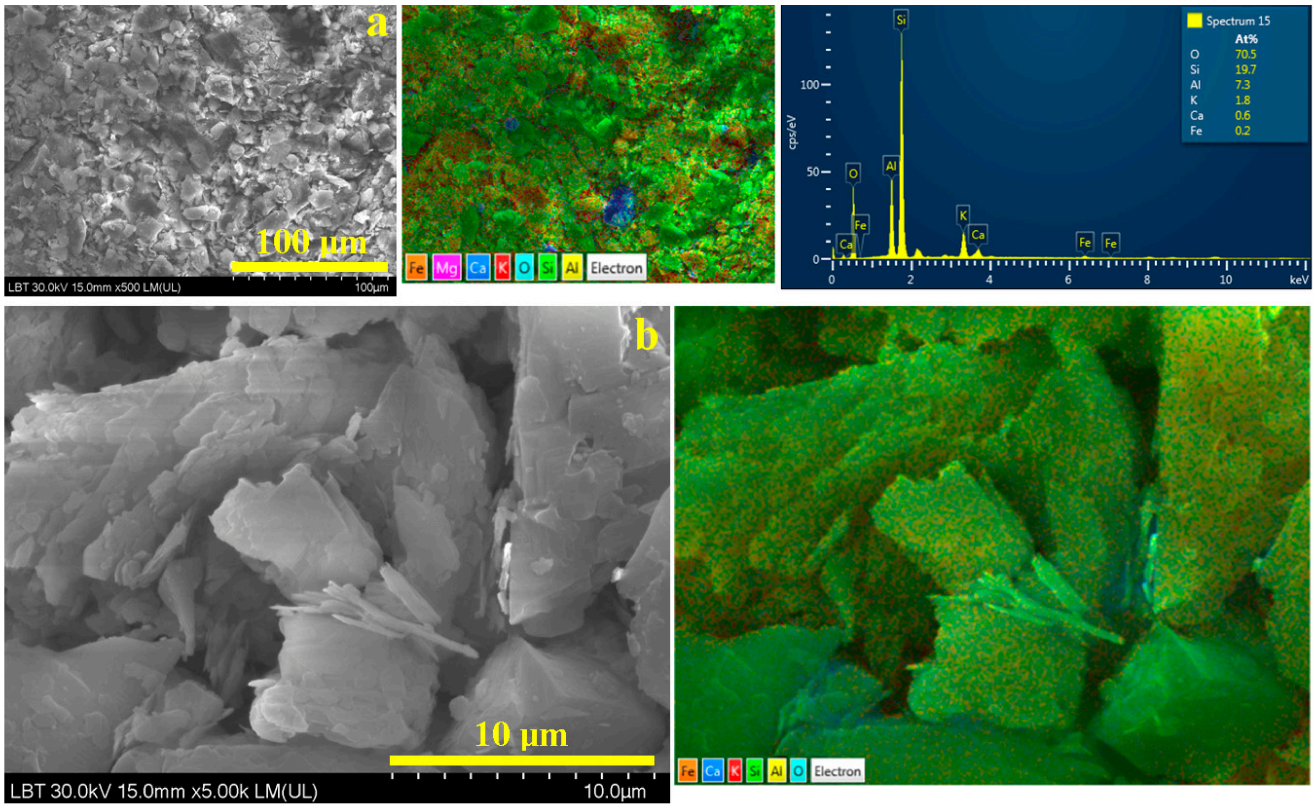


Figure 5. SEM images of the WWS sample: (**a**) SEI image of the overall microstructure, (**b**) SEI image of the microstructural detail. BSE images with elemental map and EDS spectrum are presented on the right side of SEI images.

Microstructural details in Figure 5 reveal two quartz particles in the lower corners of the images, having boulder-like shape with blunted edges, but some of them are very sharp, indicating a fresh fracture gained during the raw material milling process. The

surrounding kaolinite particles are of very good quality, revealing nice lamellar–tabular sheets with the planar size ranging from 1 to 8 µm, in good agreement with cross-polarized light observation. These are well individualized, indicating that were nicely settled down within the sediment without external forces applied onto them. Therefore, they maintain their relatively intact natural foliated aspect.

A significant technological detail regarding the future sustainable application of this type of sediment emerges from this microstructural aspect. If the intended application requires well-structured kaolinite particles at the microscopic level, then allowing this type of sediment to settle and gently collecting it represents an optimal method of valorization prior to the pressure filtration of the wastewater.

The SLR sample's overall microstructure (Figure 6a) is more compact due to the pressing filtration process. Quartz and feldspar boulder-like particles ranging from 3 to 60 µm are dispersed randomly into an embedding matrix formed by dense kaolinite particles. Iron hydroxides are finely distributed in this kaolinite matrix, but the orange spots are more firm, indicating consolidation of goethite particles, as observed by XRD.

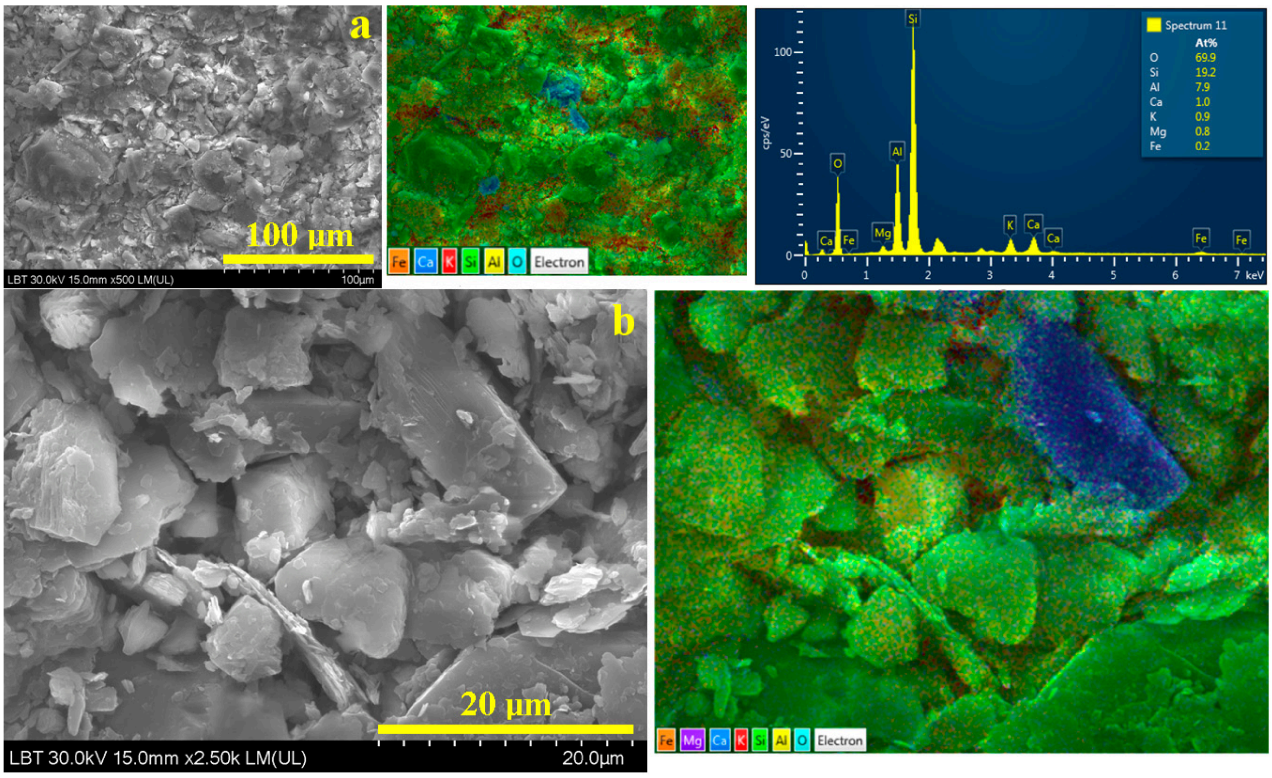


Figure 6. SEM images of the SLR sample: (**a**) SEI image of the overall microstructure, (**b**) SEI image of the microstructural detail. BSE images with elemental map and EDS spectrum are presented on the right side of SEI images.

Microstructural details in Figure 6b reveal quartz particles with partly sharp edges caused by fresh fragmentation through milling, tightly embedded by kaolinite particles with broken and altered shapes. The kaolinite foliated particles have the outermost layers broken into very fine fractions (including submicron formations) as a consequence both of the milling of raw materials and also pressing filtering. The upper fight side of Figure 6b reveals a significant anorthite particle (blue appearance in the elemental map because of its Ca content) with specific appearance, as reported in the literature [46].

Particle size distribution was quantified with Image J software, resulting in the histogram shown in Figure 7. Both samples exhibit a bimodal distribution characterized by

the predominance of fine, powdery fractions (clay) as well as the distribution of coarse quartz and feldspar particles.

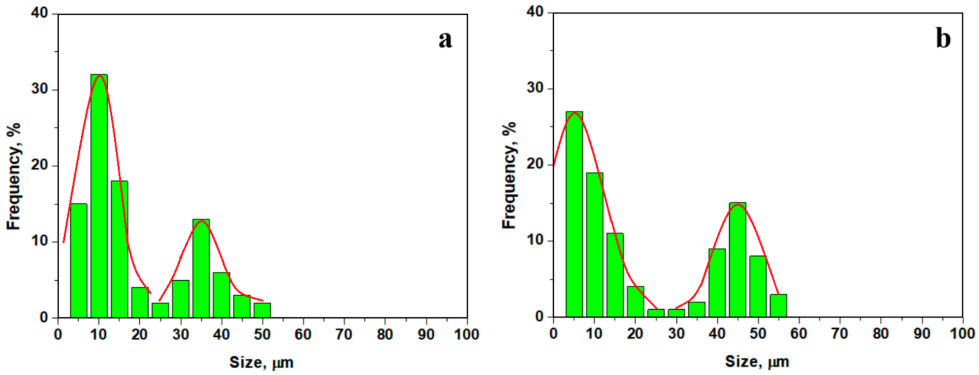


Figure 7. Particle size distribution histograms quantified with Image J software on SEM images of: (**a**) WWS and (**b**) SLR.

The coarse quartz and feldspar particles are dominated by the 35 µm fractions for WWS and the 45 µm fractions for SLR, a finding also consistent with microscopic observations under polarized light with crossed nicols. The fine fractions of the WWS sample are dominated by the 10 µm fraction (Figure 7a), whereas the ultrafine fractions (<5 µm) account for only 15%. In contrast, the SLR sample is dominated by the ultrafine fractions (<5 µm), as shown in the histogram in Figure 7b. In this sample, the 10 µm fraction is of secondary importance, accounting for just fewer than 20% of the total, a fact in good agreement with Figure 8.

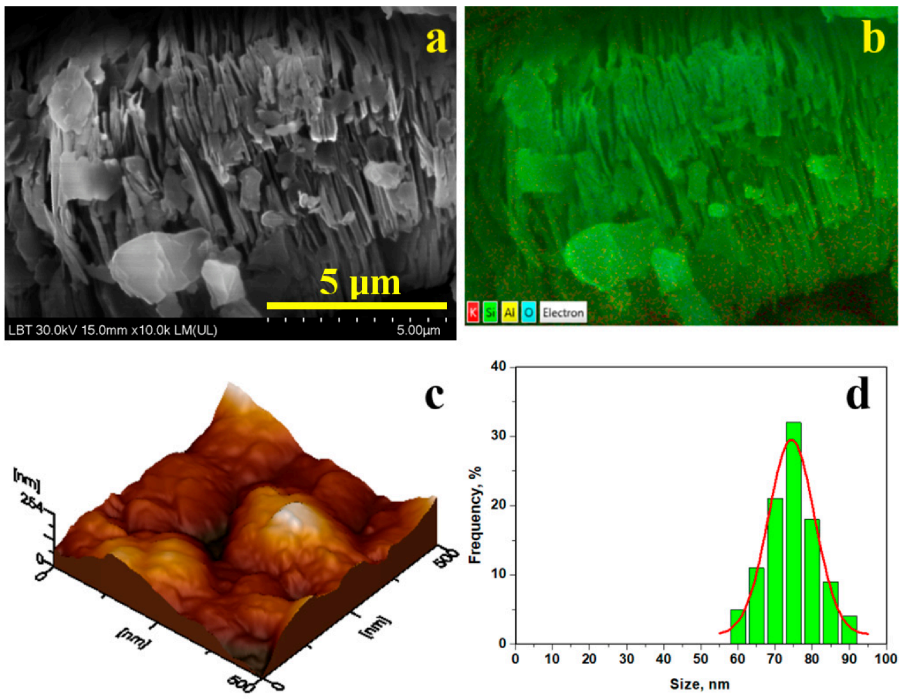


Figure 8. SLR ultra fine particles: (**a**) SEM–SEI detail taken at ×10,000 magnification, (**b**) BSE elemental map for (**a**) image, (**c**) AFM topographic image revealing nano fractions and (**d**) particle size distribution histogram.

The ultrafine fractions of SLR require further investigation. Accordingly, Figure 8a shows a highly refined structure of kaolinite particles, a feature supported by the BSE image, and the corresponding elemental distribution. Dispersing these ultrafine fractions

in an aqueous medium and subsequently adsorbing them onto a solid substrate (e.g., a glass slide) enabled AFM analysis (Figure 8b), which clearly reveals well-distributed nanoparticles having tabular–lamellar shapes. The particle size distribution histogram indicates an average size of 75 nm. This finding is in good agreement with the 68 nm crystallite size calculated for kaolinite using the Scherrer formula based on its noticeably broadened diffraction maxima.

Mineral particle rearrangements as a consequence of pressing filtration have a moderate influence on the elemental composition of the investigated samples, confirming the enrichment in fine particles of the SLR sample against WWS, as shown in Table 3. The mild decrease in quartz content within SLR compared to WWS is confirmed by a mild decrease in Si content, benefiting from a slight increase in Al content, which proves the appreciation of kaolinite.

Table 3. Sample elemental composition.

Element	Elemental Composition, at. %						
	O	**Si**	**Al**	**Ca**	**K**	**Fe**	**Mg**
WWS	70.5	19.7	7.3	0.6	1.8	0.2	-
SLR	69.9	19.2	7.9	1.0	0.9	0.2	0.8

A significant decrease in K level sustains a consistent decrease in muscovite amount in SLR, confirming the cross-polarized light and XRD investigations. Also, anorthite feldspar quantity can be appreciated more in SLR than in WWS. Overall, it means that the WWS sample is less representative of the average composition of the slurry and still depends on the interaction with the alkaline wet environment. The pressed slurry presents a better consistency of the mineral composition, although it does not fully preserve the integrity of the lamellar kaolinite particles, but increases the binding properties of the embedding matrix. Small traces of 0.8% Mg most likely occur from mild contamination of muscovite phase with biotite black mica, but far below the XRD detection limit.

Our previous study revealed that the proper moisture of ceramic wastewater slurry kaolinite matrix is about 20% using technological alkaline water (pH 10) to ensure an optimal paste for the proper distribution of the quartz granular material, suitable for pressing sustainable parts with enough mechanical strength for green applications, including reinforcing with vegetal fibers [19]. On the other hand, choosing a proper temperature to gain kaolinite dehydroxylation ensures a low carbon footprint for the moderate thermal consolidated parts [15]. Therefore, the thermal behavior of the ceramic slurry samples collected from the porcelain production must be further assessed to identify the optimal sustainable applications.

3.4. Thermal Behavior

The previously highlighted microstructural aspects reveal that porcelain ceramic sludge has significant potential, both to cause serious particulate pollution and, conversely, to be utilized in a sustainable manner. From this perspective, it is crucial to observe its behavior during heat treatment. Figure 9a displays the simultaneous TG–DTA curves of the sediment (WWS) and slurry (SLR) samples, which exhibit similar thermal behavior.

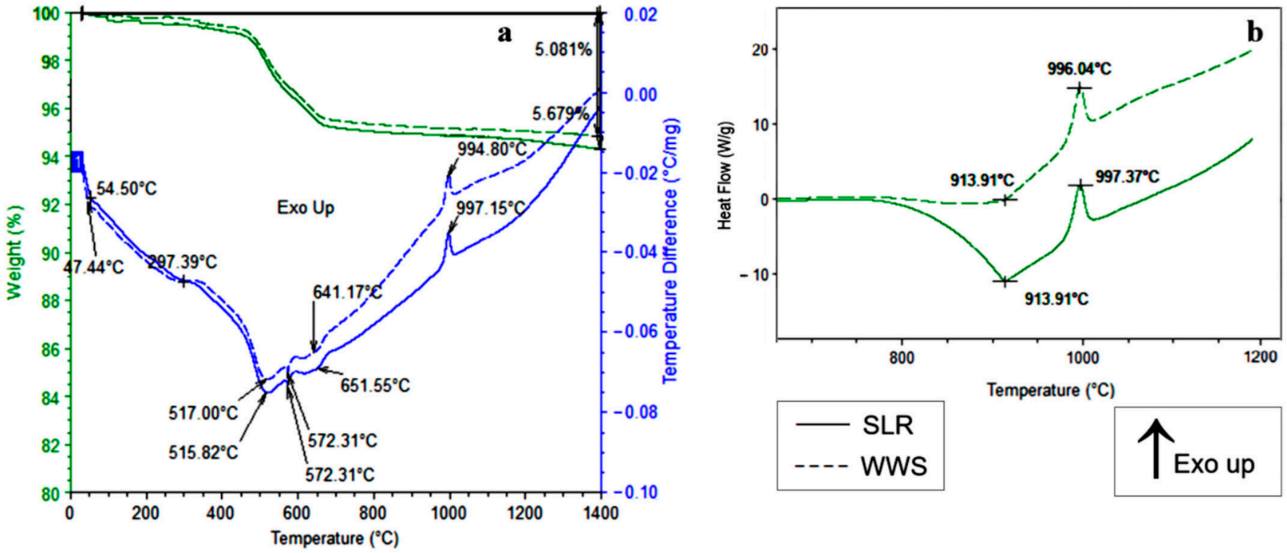


Figure 9. Thermal analysis of the SLR and WWS samples: (**a**) simultaneous thermogravimetric (TG) and differential thermal analysis (DTA) curves and (**b**) differential scanning calorimetry (DSC) curves.

A slight mass loss of 0.1606% for WWS and 0.4226% for SLR was recorded below 200 °C. This initial small mass change is assigned to the removal of physically adsorbed moisture [47]. This desorption process correlates in the DTA plot with a weak endothermic peak [48].

Over the entire course of the analysis, WWS shows a consistently higher mass loss response than SLR, which may be attributed to compositional differences between the samples resulting from their distinct collection regions; see Figure 1. It deals with the higher moisture retained in the simply collected sedimented particles compared to the pressed slurry, where the physical water is better extracted through the filtration process.

Increasing the temperature up to 700 °C, the mass loss continues to evolve, reaching 4.280% for WWS and 4.354% for SLR, respectively. This substantial mass loss is primarily attributed to the release of chemically bound water and to the dehydroxylation of kaolinite. The removal of chemically bound water appears in the DTA curve as a slight endothermic deviation near 297 °C, possibly linked to a minor structural transformation [47]. In the DTA curve, the dehydroxylation process is evidenced by an endothermic effect at approximately 517 °C [49,50], followed by the α–β quartz transformation at around 572 °C [51–54], and a broader endothermic feature near 641 °C, which may be associated with further structural rearrangements and residual dehydroxylation processes.

The simultaneous occurrence of exothermic organic matter oxidation and endothermic mineral transformations between 200 and 550 °C might alter the shape of DTA/DSC signals [50]. This overlap likely contributes to the lower dehydroxylation temperature observed at 517 °C in our sample. Reported dehydroxylation temperatures generally range from approximately 530 to 630 °C, with some studies reporting temperatures as high as 700 °C [48,52]. The endothermic event centered at about 517 °C is attributed primarily to kaolinite dehydroxylation, in agreement with the kaolinite identified by XRD. The relatively low temperature of this event may be consistent with a lower degree of structural ordering within kaolinite fine fractions of about 75 nm, evidenced by high-magnification SEM and AFM topographic images with particle size distribution histogram in Figure 8, with respect to the literature data [54].

The DTA curve shows a sharp exothermic peak at approximately 994 °C for WWS and 997 °C for SLR, which corresponds to the onset of mullite crystallization [48,52,55]. At the final temperature of 1400 °C, the cumulative mass loss reaches 5.679% for WWS,

whereas SLR shows a total mass loss of 5.081%, confirming the systematically higher mass loss behavior of WWS over the entire thermal pathway.

It is also important to note that although our samples are like those reported in the literature, beyond instrumental parameters and intrinsic material properties, the sample preparation can also affect the shape of the DTA curve. Intensive grinding is known to introduce structural defects in minerals, altering their thermal response. In our case, the sample is extremely fine due to the collection method, which may contribute to the slight shift observed in the dehydroxylation temperature.

The DSC curves, shown in Figure 9b, exhibit two distinct thermal events: an endothermic effect near 913 °C, likely associated with structural rearrangements within the dehydroxilated kaolinite interaction with the pre-existent mullite (11–12% observed by XRD), which occurs prior to the mullitization process, a fact in good agreement with our previous investigations regarding ceramic tile wastewater slurry subjected to moderate thermal consolidation [14]. In this case, it was observed that pre-existing mullite facilitated the transformation of dehydroxylated kaolinite into mullite during firing at 900 °C. This corresponds to the thermal effect observed at 913 °C. The sharp exothermic peak at 996–997 °C corresponding to mullite crystallization was also observed in DTA curves. The early-stage mullite reorganization was typically observed in recycled porcelain and ceramic tile waste [56]. This is most likely due to mullite particles pre-existing in the recirculated material, which triggers the transformation at a slightly lower temperature than would be the case for the transformation of pure dehydroxylated kaolinite. This is consistent with mineralogical microscopy observations under cross-polarized light (Figure 4).

The thermal transformations revealed by TG-DTA and DSC analyses are such that they dramatically affect the nature of the chemical bonds within the microstructure, necessitating specific analyses such as FTIR spectroscopy. The comparable mineralogical composition of the WWS and SLR samples results in very similar FTIR spectra, both before and after heat treatment, as shown in Figure 10. Although WWS seems to have slightly enhanced the absorption bands for physical adsorbed water, OH bonds are typically represented for kaolinite.

Kaolinite specific hydroxyl bonds are clearly represented in both WWS and SLR raw samples at 3692 cm^{-1}; this belongs to the stretching of outer OH bonds, while the inner OH bonds are represented by the absorption band at 3620 cm^{-1}, in good agreement with the literature [57]. Kaolinite OH bond bending occurs at 911 cm^{-1} in the FTIR spectra of both initial WWS and SLR [58].

The weak absorption band at 1434 cm^{-1} is known for C-O stretching within carbonates [59,60]. But since no carbonates were detected by XRD and no carbon was detected during SEM-EDX elemental measurements, it most likely occurs because of other exogenous contamination. Small amounts of Mg detected in SLR samples accounted for mild contamination of muscovite, with magnesian biotite confirmed by the appearance of this band related to NH_4^+ ions occurring in the natural biotite [61,62].

Silicate absorption bands are dominated by SI-O in-plane stretching at 1033 cm^{-1} [63], but a tight shoulder band is slightly detached on the left side at 1112 cm^{-1}, which corresponds to the tetrahedral and octahedral layers within kaolinite bonded to the apical oxygen. Al–O stretching is represented by the shoulder band at 882 cm^{-1} and transition of Al ions within the tetrahedral positions at 779 cm^{-1} [58], while Si-O-Al bending occurs at 534 cm^{-1} [57]. Very close to this last position, the absorption band can be found for Fe-O at 520 cm^{-1} [64].

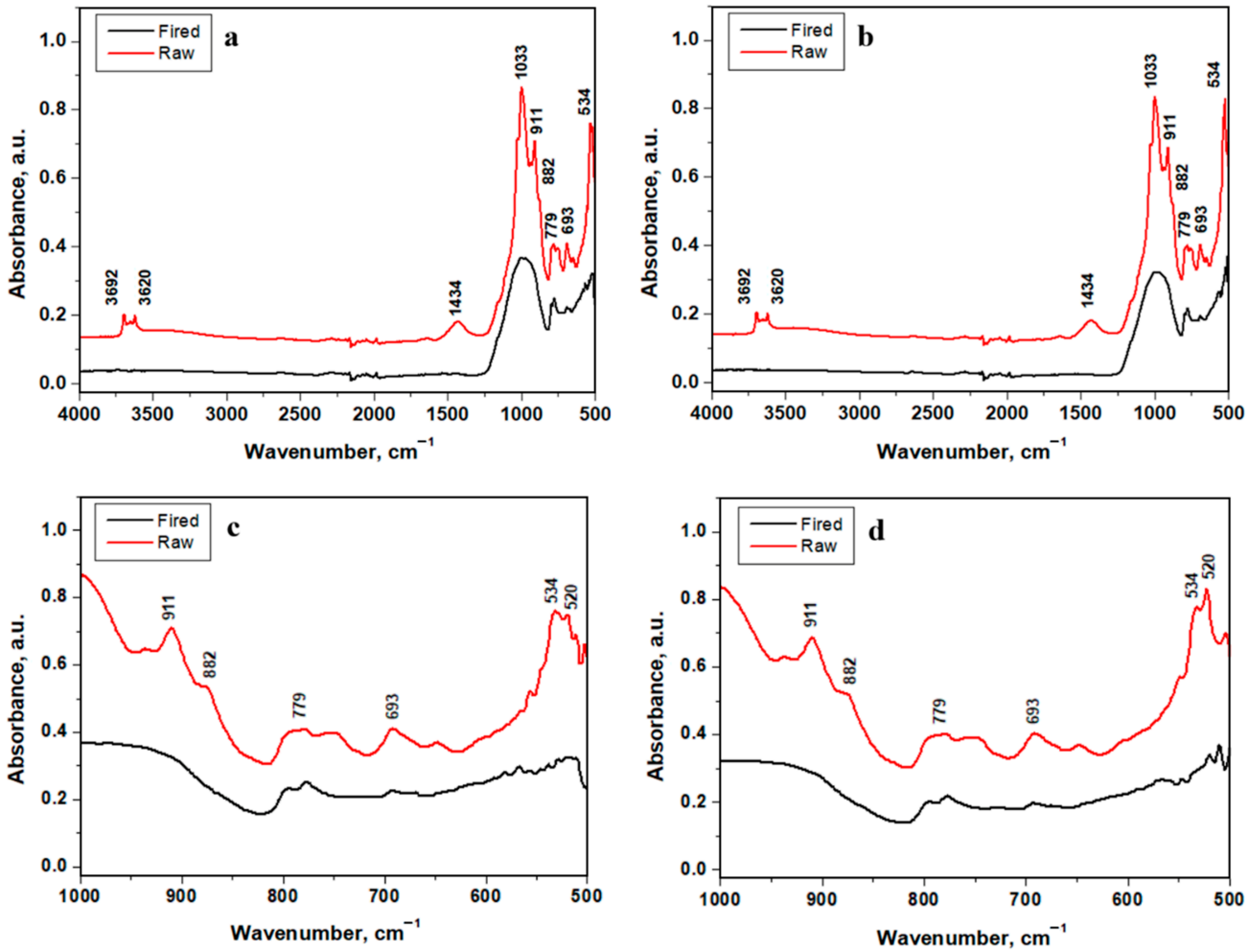


Figure 10. FTIR spectra before and after thermal analysis for: (**a**) WWS and (**b**) SLR. Spectra details in the range of 500–1000 cm^{-1} are displayed as follows: for (**a**) is presented in (**c**) and for (**b**) in (**d**).

Specific absorption bands (stretching and bending) of OH bonds associated with kaolinite disappear after the sample firing. Kaolinite dehydroxylation implies the merging of the main absorption bands into a broadened one with the peak at 1033 cm^{-1} because of disordering of the kaolinite crystal lattice, which lacks the apical oxygen within its structure [57]. It is noteworthy that the Fe-O bond within goethite and lepidocrocite is significantly affected by the thermal treatment but it does not remove its component, which most likely occurs in pronounced staining of the densified kaolinite matrix and subsequently embedded into the amorphous porcelain glassy phases.

Thermal analyses correlated with FTIR spectroscopy reveal key aspects of the material under investigation. The first is the loss of physically bound water, followed by the dehydroxylation of kaolinite. These significant stages are succeeded by a phase of progressive structural breakdown of the kaolinite, involving the gradual densification of the matrix; the matrix tightens increasingly around the quartz and feldspar particles, thereby enhancing the cohesion of the resulting composite. The transition of alpha quartz into beta quartz is representative of the thermal behavior of the material, but it is a reversible process that does not affect the final product unless it is fired under high temperature.

Consequently, the temperature range between 600 and 800 degrees Celsius is of particular interest for the efficient thermal consolidation of the material, offering a sustainable solution by reducing the energy consumption that would otherwise be required for high-temperature firing.

4. Discussion

Sustainability is a complex concept encompassing several environmental aspects, such as minimizing waste emissions from technological flows, minimizing industrial waste sent to disposal sites [65,66], and optimizing technological processes through the circular economy [67,68]. A comprehensive analysis of the technological workflows specific to the production of porcelain parts and tiles reveals that various material particles resulting from wet or dry processes end up in industrial wastewater, primarily through the washing of components at various stages [69]. As demonstrated by the complex physicochemical analyses performed, iron hydroxides contaminate the fine fractions of the kaolinitic matrix in significant amounts of 7–9%. Since the maximum allowable amount of iron hydroxides in raw material is 1% [19,20], this prevents the reuse of this ceramic waste within the same technological process, rendering it unsuitable according to the principles of direct sustainability. Porcelain powder waste resulting from the grinding process, molding rejects, or defective fired pieces can be ground and directly recirculated; however, sludge collected from process wastewater cannot be reused in this way, as it leads to the formation of brown spots [16,17], which is unacceptable for pieces where aesthetic appearance is paramount.

There is less literature information regarding the sustainable approach of porcelain wastewater slurry, with most references indicating porcelain slurries used for 3D printing [70,71]. This is not a waste material, but a precise composition designed for precise detail parts. On the other hand, Ruviaro uses metakaolin and water treatment plant sludge to achieve geopolymers [72] but does not address the slurry resulting from the technological wastewater from porcelain production. The situation is very similar to the general sustainable approach within environmental decarbonation through the replacement of Portland cement with various geopolymer compositions that consume various particulate matter wastes like red mud and fly ash [11–13].

The unsustainable traditional approach leads to the disposal of this sludge in waste piles that are becoming increasingly massive and difficult to manage. European Union waste deposition regulation imposes handling and storage fees for such slurry, ranging from €280 to €500 per ton, including transport to the disposal site [73]. Such environmental expenses influence the final cost of the product; sustainable management of the resulting slurry would spare these expenses, making the production cost more attractive.

Deposition is carried out using a wet method, yet over time, veritable mountains of such fine, powdery waste accumulate; these must be kept constantly wet to prevent surface drying and the release of hazardous particles into the air. Our findings clearly reveal that both WWS and SLR can release PM10 emissions containing predominantly quartz and feldspar and clay fractions (kaolinite and muscovite), releasing predominantly PM2.5, known for hazardous potential regarding silicosis and asthma [22,24]. Microstructural details taken by SEM under high magnification revealed the finest kaolinite particles having about 1 μm diameter and below, fitting the PM1 range, which is directly related to lung cancer if people are exposed for longer lengths of time [27,74]. These particles, as observed, have tabular shapes with sharp edges, which act as micro knives under pulmonary alveoli during movement of the chest during breathing, facilitating the additional organic pollution to penetrate directly into the oxygenated blood flow. Such a situation is not acceptable, and a sustainable approach is to diminish these slurry dumps through their consumption as raw material for a related sub-product.

Our physicochemical findings reveal that iron hydroxides do not affect the structural ability of the slurry to generate hard ceramic bodies under certain treatment if the aesthetic aspect is not required or brown spotted aspect can be considered fashionable. The correlation with thermal analysis indicates three possible pathways for sustainable recycling of this slurry.

Instead of iron hydroxide dispersion, the overall aspect of WWS and SLR is white and the first sustainable approach can be related to the release of physical water through mild drying followed by a consolidation up to 300 °C, which allows manufacturing nice wall decorations for indoor house design. This might imply the application of varnish to protect the microstructure of pieces. Such decorations require low mechanical strength of about 1–3 MPa.

The very interesting temperature range between kaolinite dehydroxylation and its mullitization, briefly between 600 and 800 °C, is very attractive for a moderate thermal treatment, ensuring the proper consolidation of the kaolinite matrix over the quartz and feldspar granular material, forming a dense composite material. Release of both physically and chemically bonded water ensures proper resistance against hygroscopicity. Thus, the mild thermal consolidated parts can be exposed to the outdoor environment. It is expected that such a consolidated material has compressive strength between 6 and 15 MPa, comparable to high-quality bricks [15]. It allows using this consolidated composition for facades of building parts, which are less often subjected to compressive force, or other useful construction parts. Such parts can be of cellular ceramics, like those produced by the powder resulting from porcelain polishing [56]. Adding 30% of porcelain polishing waste to ceramic paste reduces the mullite crystallization activation energy to 493 ± 18 kJ/mol, when compared to paste without this addition, having an activation energy of 780 ± 43 kJ/mol. Increasing the polishing residue amount to 50%, the activation energy decreases to 530 ± 30 kJ/mol [75]. The activation energy decrease is in good agreement with the decreasing mullitization temperature observed in our slurry samples.

The complete mullitization of the material would ensure a dense ceramic body with high mechanical properties and weathering resistance, but achieving temperatures around 900 °C requires more energy and more fuel, which increases the product carbon footprint and reduces its sustainability, unless certain technological applications would require such ceramic parts produced from SLR sample, justifying the energy consumption.

The current research has carried out a complex physicochemical investigation of the ceramic slurry resulting from porcelain manufacturing technological wastewater, revealing the main sustainable strategies for the reduction of dumping and mitigation of particulate matter hazards associated with these wastes. The identified sustainable pathways will be explored by continuing this research to investigate microstructural changes within the thermal consolidation and mechanical behavior under compressive strength.

The conventional approach involves neutralizing the pH of the water resulting from filtration and discharging it into the sewer system. However, given the advanced removal of fine particles—including iron hydroxides (which are insoluble in water)—the water can be recirculated within the system. Consequently, the potential route is indicated by a dashed green line in Figure 1; this route is applicable to the raw material preparation stages and the grinding process. This results in a significant reduction in freshwater consumption, thereby enhancing the sustainability of the technological process. For instance, Italian ceramic manufacturers report a high level of wastewater recirculation, about 99%, highlighting that every drop of water matters [76]. Such advanced wastewater filtering is ensured by primary sedimenting of the coarse fraction followed by pressing filtering [77], similar to our investigated technological process.

Certain limitations of the current research reside in the lack of in-depth knowledge regarding technological parameters used in manufacturing processes, which are connected to legal requirements and could not be consulted. Since the investigated production line is small, it certainly affects the sample size (n = 3 for water samples and n = 6 for slurry samples). On the other hand, this limitation has a great benefit because we observe that revealing the complex composition of the slurry and its behavior is enough to determine

sustainable strategies which are not directly connected to the mother technological process. If the sustainable process is to be outsourced by other manufacturers, they can buy the slurry from the dump as cheap raw material.

5. Conclusions

The ceramic slurry recovered from the technological wastewater from porcelain manufacturing is a rich mineral particulate matter dispersion dominated by granular material formed by 29% quartz and 15% feldspar surrounded by a dense dispersion of fine fractions of clay (kaolinite 27% with traces of 8% muscovite).

Quartz and feldspar have significant fractions of PM10, while kaolinite predominates in PM2.5 and PM1 fractions (including ultra-fine nanoparticles of about 75 nm, as resulting from AFM investigation). This particulate matter represents a high environmental hazard if released into the atmosphere. Therefore, their mitigation and reduction of their dumping are the first stages towards a sustainable approach.

A low-temperature sustainable approach implies the usage of slurry for indoor design parts subjected to mild drying and additional protection with outer varnish. It has the benefit of nice aspects and low energy consumption.

Moderate temperature treatment from 600 to 800 °C ensures a proper dehydroxylation of the kaolinite matrix, ensuring a consolidated composite structure suitable for outdoor facade building materials as a potential sustainable strategy using lower energy consumption, which makes it possible to achieve the desired properties.

The presence of fine and ultra-fine fractions of kaolinite facilitates the beginning of the mullitzation process at lower temperatures than usual: 994 °C (WWS) and 997 °C (SLR).

The sustainable recycling strategies identified based on physicochemical results are designed to reduce production costs by eliminating the component attributable to slurry landfilling fees.

Filtered wastewater recirculation would increase the sustainability of the technological process, sparing freshwater usage and protecting the natural water sources.

Author Contributions: Conceptualization, S.E.A. and I.P.; methodology, S.E.A., R.A.M. and I.P.; software, G.B. and M.R.F.; validation, S.E.A. and R.A.M.; formal analysis, I.P. and R.A.M.; investigation, S.E.A., L.B.T., G.B., R.A.M., M.R.F. and I.P.; resources, S.E.A.; data curation, I.P. and M.R.F.; writing—original draft preparation, S.E.A., R.A.M. and I.P.; writing—review and editing, I.P. and R.A.M.; visualization, L.B.T. and I.P.; supervision, S.E.A. and I.P.; project administration, S.E.A. and I.P. All authors have read and agreed to the published version of the manuscript.

Funding: This research received no external funding.

Institutional Review Board Statement: Not applicable.

Informed Consent Statement: Not applicable.

Data Availability Statement: The original contributions presented in the study are included in the article.

Conflicts of Interest: The authors declare no conflicts of interest.

Abbreviations

The following abbreviations are used in this manuscript:

AFM	Atomic Force Microscopy
EDS	Energy Dispersive Spectroscopy
MOM	Mineralogical Optical Microscopy

PM	Particulate matter
SEM	Scanning Electron Microscopy
XRD	X-ray Diffraction

References

1. Li, J.; Wu, A.; Long, D.; Lin, Z.; Gao, J.; Fang, T.; Li, Q.; Zhang, M. A Preliminary Investigation on the Identification of Artificial Irradiation in Thermoluminescence Pre-Dose Dating of Ancient Chinese Porcelain. *Crystals* **2025**, *15*, 503. [CrossRef]
2. Zhou, B.; Ma, Q.; Li, Z.; Chen, J. Corrosion Research on Ru Porcelain Glazes Excavated at Qingliangsi, Baofeng, China. *Coatings* **2023**, *13*, 1011. [CrossRef]
3. Colomban, P.; Simsek Franci, G.; Gerken, M.; Gironda, M.; Mesqui, V. Non-Invasive On-Site XRF and Raman Classification and Dating of Ancient Ceramics: Application to 18th and 19th Century Meissen Porcelain (Saxony) and Comparison with Chinese Porcelain. *Ceramics* **2023**, *6*, 2178–2212. [CrossRef]
4. Beauvoit, E.; Cantin, N.; Lemasson, Q.; Chapoulie, R.; Ben Amara, A. Archaeometric Characterization of the Industrial Production of Porcelains in the Vieillard & Co. Manufactory (Bordeaux, France, 19th Century). *Materials* **2022**, *15*, 5311. [CrossRef] [PubMed]
5. World Production and Consumption of Ceramic Tiles. 2024. Available online: https://www.ceramicworldweb.com/en/economics-and-markets/world-production-and-consumption-ceramic-tiles-2024 (accessed on 9 July 2026).
6. Ceramics Tile Industry Statistics. Available online: https://worldmetrics.org/ceramics-tile-industry-statistics/ (accessed on 9 July 2026).
7. Ilyina, V.; Klimovskaya, E.; Bubnova, T. Ceramic Materials Based on Clay and Soapstone Waste: Thermo-Mechanical Properties and Application. *Minerals* **2023**, *13*, 1376. [CrossRef]
8. Lourenco Alves, C.; de Oliveira Martins Müller, J.; de Noni, A., Jr.; Heinrich, S. Challenges and opportunities for increase sustainability and energy efficiency in ceramic tile industry. *Int. J. Appl. Ceram. Technol.* **2025**, *22*, e15097. [CrossRef]
9. Guerrero-Rodríguez, N.F.; Ramírez-Rivera, F.A.; Ramos Ciprian, R.D. Green Hydrogen for Critical-Load Restoration in High-Renewable Power Systems: Energy Not Served Reduction, Economic Value, and Carbon-Resilience Assessment. *Clean Technol.* **2026**, *8*, 102. [CrossRef]
10. Mihetec, M.; Pokrovac, M.; Šoša, Z.; Stunjek, G.; Krajačić, G. Green Industrial Zones and Ports: A 100% Renewable Energy Transition Model. *Sustainability* **2026**, *18*, 6910. [CrossRef]
11. Serafim, A.; Antunes, E.; Dalfré, G.; Almeida, R.d. Porcelain Polishing Residue as a Supplementary Cementitious Material in Self-Compacting Concrete: Pozzolanic Activity and Performance Assessment. *Powders* **2026**, *5*, 10. [CrossRef]
12. Pontes, I.C.; Neto, J.A.d.S.; Lemos, M.H.C.; dos Anjos, M.A.S.; Pederneiras, C.M.; Dutra, R.P.S. Effect of High Levels of Pyroexpansive Agents from Porcelain Polishing Waste on Artificial Lightweight Aggregates Produced with Red Clay. *Buildings* **2026**, *16*, 940. [CrossRef]
13. Martins de Oliveira, V.S.; Neto, J.A.d.S.; Nascimento, G.L.d.; Anjos, M.A.S.d.; Dutra, R.P.S.; Pederneiras, C.M. Evaluating Porcelain Polishing Waste as a Pyro-Expansive Agent in Clay Formulations for Sustainable Lightweight Aggregates. *Sustainability* **2025**, *17*, 7385. [CrossRef]
14. Avram, S.E.; Birle, B.V.; Tudoran, L.B.; Borodi, G.; Petean, I. Investigation of Used Water Sediments from Ceramic Tile Fabrication. *Water* **2024**, *16*, 1027. [CrossRef]
15. Avram, S.E.; Birle, B.V.; Cosma, C.; Tudoran, L.B.; Moldovan, M.; Cuc, S.; Borodi, G.; Petean, I. Ecological Building Material Obtained Through the Moderate Thermal Consolidation of Ceramic Slurry Collected from Industrial Waste Waters. *Materials* **2025**, *18*, 1715. [CrossRef] [PubMed]
16. Wang, Y.; Yu, S.; Chu, J.; Chen, D.; Chen, J. Study on the copper and iron coexisted coloring glaze and the mechanism of the fambe. *J. Eur. Ceram. Soc.* **2018**, *38*, 3681–3688. [CrossRef]
17. Mourou, C.; Zamorano, M.; Ruiz, D.P.; Martín-Morales, M. Characterization of ceramic tiles coated with recycled waste glass particles to be used for cool roof applications. *Constr. Build. Mater.* **2023**, *398*, 132489. [CrossRef]
18. Barrachina, E.; Calvet, I.; Fraga, D.; Carda, J.B. Ceramic porcelain stoneware production with Spanish clays purified by means of the removal of iron compounds and organic matter using physical methods. *Appl. Clay Sci.* **2017**, *143*, 258–264. [CrossRef]
19. Pereira, O.C.; Bernardin, A.M. Ceramic colorant from untreated iron ore residue. *J. Hazard. Mater.* **2012**, *233–234*, 103–111. [CrossRef] [PubMed]
20. Galos, K. Composition and ceramic properties of ball clays for porcelain stoneware tiles manufacture in Poland. *Appl. Clay Sci.* **2011**, *51*, 74–85. [CrossRef]
21. Avram, S.E.; Tudoran, L.B.; Borodi, G.; Filip, M.R.; Ciotlaus, I.; Petean, I. Physicochemical Aspects Regarding the Sustainable Conversion of Carwash Slurry as Coverage Admixture for Landfills. *Sustainability* **2025**, *17*, 2906. [CrossRef]
22. Javier, C.; Belur, P.; Gandhi, S. accelerated simple silicosis in an immigrant: Engineered stone worker in California. *Chest* **2025**, *168*, A5837–A5838. [CrossRef]

23. Kyrmanidou, M.; Smaraidos, I.; Kampouras, A. Association Between Air Pollution and Childhood Asthma: A Systematic Review of Recent Evidence. *Adv. Respir. Med.* **2026**, *94*, 31. [CrossRef] [PubMed]
24. Martins Costa Gomes, G.; Collison, A.M.; Murphy, V.E.; Brew, B.K.; Robinson, P.D.; Morgan, G.G.; Gopi, K.; Gibson, P.G.; Karmaus, W.; Mattes, J. Early Gestational Wildfire-Related $PM_{2.5}$ Exposure Is Associated with Lung Function in Offspring of Mothers with Asthma. *Int. J. Environ. Res. Public Health* **2026**, *23*, 314. [CrossRef] [PubMed]
25. de Almeida Neto, A.B.; de Moura, F.R.; Bonifácio, A.d.S.; da Silva, V.M.; Brum, R.d.L.; Tavella, R.A.; Fernandes, R.C.; Mariano, G.L.; da Silva Júnior, F.M.R. $PM_{2.5}$ and Lung Cancer: An Ecological Study (2014–2023) Using Data from Brazilian Capitals. *Atmosphere* **2026**, *17*, 175. [CrossRef]
26. Prommana, S.; Intarasit, S.; Thongyim, S.; Yabueng, N.; Chantara, S.; Sattayawat, P.; Panya, A.; Inwongwan, S. Biomass-Haze PM2.5 from Northern Thailand Drives Genotype-Specific Oxidative Stress and Transcriptomic Remodeling in Non-Small-Cell Lung Cancer Cells. *Toxics* **2026**, *14*, 21. [CrossRef] [PubMed]
27. Guo, H.; Wei, J.; Li, X.; Ho, H.C.; Song, Y.; Wu, J.; Li, W. Do socioeconomic factors modify the effects of PM_1 and SO_2 on lung cancer incidence in China? *Sci. Total Environ.* **2021**, *756*, 143998. [CrossRef] [PubMed]
28. Bao, Q.; Cheng, H.; Wang, Y.; Liang, S. Mechanism of hydrothermal illite clay mineralization in the southern Ordos Basin, central China. *Ore Geol. Rev.* **2026**, *189*, 107129. [CrossRef]
29. Simpson, M.P.; Morales, A.G.; Chambefort, I.; Alcaraz, S.; Moribe, S.; Milicich, S.D.; Sepulveda, F.; Hedenquist, J.W. The Rotokawa geothermal system, New Zealand: Hydrothermal minerals and punctuated evolution. *J. Volcanol. Geotherm. Res.* **2026**, *477*, 108665. [CrossRef]
30. Sinani, B.; Boev, B.; Reka, A.A.; Sinani, B.; Boev, I. Distribution of Naturally Occurring Asbestos in the Mitrovica Region: Geochemical and Mineralogical Characterization. *Geosciences* **2025**, *15*, 335. [CrossRef]
31. Watteau, F.; Morel, J.L.; Liu, C.; Tang, Y.; Huot, H. Technosol Micromorphology Reveals the Early Pedogenesis of Abandoned Rare Earth Element Mining Sites Undergoing Reclamation in South China. *Minerals* **2025**, *15*, 514. [CrossRef]
32. Goga, F.; Bortnic, R.A.; Avram, A.; Zagrai, M.; Barbu Tudoran, L.; Mereu, R.A. The Effect of Ni^{2+} Ions Substitution on Structural, Morphological, and Optical Properties in $CoCr_2O_4$ Matrix as Pigments in Ceramic Glazes. *Materials* **2022**, *15*, 8713. [CrossRef] [PubMed]
33. Zagrai, M.; Gavrea, R.C.; Macavei, S.; Dehelean, A.A.; Popa, A.; Soran, M.L.; Mereu, R.A. Glass-Forming Ability, Chemical Durability, and Structural Properties of Lead Dioxide-Silicate Glass System. *Crystals* **2024**, *14*, 436. [CrossRef]
34. Wang, B.; Stephen, S.J.; Vashishth, D. Identification of water compartment in bone using ATR-FTIR spectroscopy. *Spectrochim. Acta Part A Mol. Biomol. Spectrosc.* **2026**, *349*, 127360. [CrossRef] [PubMed]
35. Segnit, E.R.; Holland, H.D.; Biscardi, C.J. The solubility of calcite in aqueous solutions—I The solubility of calcite in water between 75° and 200° at CO_2 pressures up to 60 atm. *Geochim. Cosmochim. Acta* **1962**, *26*, 1301–1331. [CrossRef]
36. Cornu, S.; Montagne, D.; Vasconcelos, P.M. Dating constituent formation in soils to determine rates of soil processes: A review. *Geoderma* **2009**, *3–4*, 293–303. [CrossRef]
37. Schwertmann, U.; Taylor, R.M. The Influence of Silicate on the Transformation of Lepidocrocite to Goethite. *Clays Clay Miner.* **1972**, *20*, 159–164. [CrossRef]
38. Konan, K.L.; Peyratout, C.; Bonnet, J.P.; Smith, A.; Jacquet, A.; Magnoux, P.; Ayrault, P. Surface properties of kaolin and illite suspensions in concentrated calcium hydroxide medium. *J. Colloid Interface Sci.* **2007**, *307*, 101–108. [CrossRef] [PubMed]
39. Ma, M. The Dispersive Effect of Sodium Silicate on Kaolinite Particles in Process Water: Implications for Iron-Ore Processing. *Clays Clay Miner.* **2011**, *59*, 233–239. [CrossRef]
40. Bačkalić, Z.; Vasić, M.V.; Holló, B.B.; Jovanović, D.; Sremac, S.; Awoyera, P. From lab to industry: Analysing the performance of ceramic batch modified with sodium silicate and phosphoric acid-based additive in ceramic floor tile production. *Next Mater.* **2025**, *8*, 100891. [CrossRef]
41. García-Vera, V.E.; Tenza-Abril, A.J.; Lanzón, M. The effectiveness of ethyl silicate as consolidating and protective coating to extend the durability of earthen plasters. *Constr. Build. Mater.* **2020**, *236*, 117445. [CrossRef]
42. Tangboriboon, N.; Changkhamchom, S.; Sirivat, A. Effect of embedding eggshells to form calcium feldspar as flux in porcelain via slip casting process for bio-dental and medical applications. *Mater. Technol.* **2020**, *35*, 452–462. [CrossRef]
43. Das, S.K.; Dana, K. Differences in densification behaviour of K- and Na-feldspar-containing porcelain bodies. *Thermochim. Acta* **2003**, *406*, 199–206. [CrossRef]
44. Harabi, A.; Guerfa, F.; Harabi, E.; Benhassine, M.T.; Foughali, L.; Zaiou, S. Preparation and characterization of new dental porcelains, using K-feldspar and quartz raw materials. Effect of B_2O_3 additions on sintering and mechanical properties. *Mater. Sci. Eng. C* **2016**, *65*, 33–42. [CrossRef] [PubMed]
45. Huang, Q.; Wang, C.; Shan, Q. Quantitative Deviation of Nanocrystals Using the RIR Method in X-ray Diffraction (XRD). *Nanomaterials* **2022**, *12*, 2320. [CrossRef] [PubMed]

46. Orynbekov, Y.; Zhumadilova, Z.; Kuldeyev, E.; Tolegenova, A.; Zhuginissov, M.; Zhagifarov, A.; Nurlybayev, R.; Tengebayev, N. Influence of Waste Glass and Silica Fume Additives on the Properties and Microstructure of Clay-Based Ceramic Materials. *Appl. Sci.* **2026**, *16*, 6575. [CrossRef]
47. N. Analyzing & Testing. Thermal Analysis of Kaolin. Available online: https://analyzing-testing.netzsch.com/en/application-literature/thermal-analysis-of-kaolin (accessed on 14 July 2026).
48. Gasparini, E.; Tarantino, S.C.; Ghigna, P.; Riccardi, M.P.; Cedillo-González, E.I.; Siligardi, C.; Zema, M. Thermal dehydroxylation of kaolinite under isothermal conditions. *Appl. Clay Sci.* **2013**, *80–81*, 417–425. [CrossRef]
49. Ptáček, P.; Šoukal, F.; Opravil, T.; Nosková, N.; Havlica, J.; Brandštetr, J. The non-isothermal kinetics analysis of the thermal decomposition of kaolinite by Effluent Gas Analysis technique. *Powder Technol.* **2010**, *203*, 272–276. [CrossRef]
50. Kaljuvee, T.; Štubňa, I.; Somelar, P.; Mikli, V.; Kuusik, R. Thermal behavior of some Estonian clays and their mixtures with oil shale ash additives. *J. Therm. Anal. Calorim.* **2014**, *118*, 891–899. [CrossRef]
51. Karunadasa, K.S.; Manoratne, C.; Pitawala, H.; Rajapakse, R. The composition, unit cell parameters and microstructure of quartz during phase transformation from α to β as examined by in-situ high-temperature X-ray powder diffraction. *J. Phys. Chem. Solids* **2018**, *117*, 131–138. [CrossRef]
52. Smykatz-Kloss, W. *Differential Thermal Analysis: Application and Results in Mineralogy Minerals, Rocks and Mountains*; Springer: Berlin, Germany; New York, NY, USA, 1974; Volume 11.
53. Rambaldi, E.; Esposito, L.; Tucci, A.; Timellini, G. Recycling of polishing porcelain stoneware residues in ceramic tiles. *J. Eur. Ceram. Soc.* **2007**, *27*, 3509–3515. [CrossRef]
54. Smykatz-Kloss, W. Application of differential thermal analysis in mineralogy. *J. Therm. Anal.* **1982**, *23*, 15–44. [CrossRef]
55. Wang, H.Y.; Zhang, X.X.; Yang, S.Y.; Liu, C.; Luo, L.Q. Separation of alumina and silica from metakaolinite by reduction roasting−alkaline leaching process: Effect of $CaSO_4$ and CaO. *Trans. Nonferrous Met. Soc. China* **2022**, *32*, 999−1009. [CrossRef]
56. Sousa, I.V.; Nieves, L.J.J.; Dal-Bó, A.G.; Bernardin, A.M. Valorization of porcelain tile polishing residue in the production of cellular ceramics. *Clean. Eng. Technol.* **2022**, *6*, 100381. [CrossRef]
57. Ptáček, P.; Kubátová, D.; Havlica, J.; Brandštetr, J.; Šoukal, F.; Opravil, T. The non-isothermal kinetic analysis of the thermal decomposition of kaolinite by thermogravimetric analysis. *Powder Technol.* **2010**, *204*, 222–227. [CrossRef]
58. Tarte, P. Infra-red spectra of inorganic aluminates and characteristic vibrational frequencies of AlO4 tetrahedra and AlO6 octahedra. *Spectrochim. Acta Part A Mol. Spectrosc.* **1967**, *23*, 2127–2143. [CrossRef]
59. Kiefer, J.; Stärk, A.; Kiefer, A.L.; Glade, H. Infrared Spectroscopic Analysis of the Inorganic Deposits from Water in Domestic and Technical Heat Exchangers. *Energies* **2018**, *11*, 798. [CrossRef]
60. Varrica, D.; Tamburo, E.; Vultaggio, M.; Di Carlo, I. ATR–FTIR Spectral Analysis and Soluble Components of PM_{10} And $PM_{2.5}$ Particulate Matter over the Urban Area of Palermo (Italy) during Normal Days and Saharan Events. *Int. J. Environ. Res. Public Health* **2019**, *16*, 2507. [CrossRef] [PubMed]
61. Busigny, V.; Cartigny, P.; Philippot, P.; Javoy, M. Quantitative analysis of ammonium in biotite using infrared spectroscopy. *Am. Mineral.* **2004**, *89*, 1625–1630. [CrossRef]
62. Yang, Z.; He, M.; Wu, S.; Yang, M.; Peng, B. Near-Infrared Spectroscopic Study of Biotite–Phlogopite (Mg# = 30~99): OH-Stretching Modes and Mg# Content Prediction Equation. *Crystals* **2024**, *14*, 336. [CrossRef]
63. Koupadi, K.; Boyatzis, S.C.; Roumpou, M.; Kalogeropoulos, N.; Kotzamani, D. Organic Remains in Early Christian Egyptian Metal Vessels: Investigation with Fourier Transform Infrared Spectroscopy and Gas Chromatography–Mass Spectrometry. *Heritage* **2021**, *4*, 3611–3629. [CrossRef]
64. Cui, H.; Ren, W.; Lin, P.; Liu, Y. Structure control synthesis of iron oxide polymorph nanoparticles through an epoxide precipitation route. *J. Exp. Nanosci.* **2013**, *8*, 869–875. [CrossRef]
65. Martínez Ángeles, H.; Navarro Rubio, C.A.; Ríos Moreno, J.G.; Garcia-Barajas, M.G.; Carrillo-Serrano, R.V.; Garduño Aparicio, M.; Obregón-Biosca, S.; Trejo Perea, M. Solid Waste Disposal: A Systematic Review of Practices, Impacts and Determinants. *Clean Technol.* **2026**, *8*, 62. [CrossRef]
66. Dunca, E.-C.; Ioniță, M.-F.; Radu, S.M. Soil Contamination and Related Ecological Risks: Complex Analysis of the Defor Petrila Tailings Dump, Romania. *Land* **2025**, *14*, 1492. [CrossRef]
67. Dassanayake, C.; Mashaan, N.S.; Galagedara, R. Waste Material Utilization in Civil Engineering Applications: Advances, Challenges, and Future Directions—A Scoping Review. *Materials* **2026**, *19*, 3154. [CrossRef] [PubMed]
68. Lychev, A.V.; Ratner, S.V. The Evolution of Data Envelopment Analysis Models for Circular Economy Performance Assessment. *Algorithms* **2026**, *19*, 585. [CrossRef]
69. Javed, S.; Conte, S.; Molinari, C.; Rosa, R.; Ferrari, A.M.; Dondi, M.; Zanelli, C. Strategies and pathways to improve circularity in ceramic tile production. *J. Clean. Prod.* **2025**, *517*, 145788. [CrossRef]
70. Lima, P.; Zocca, A.; Acchar, W.; Günster, J. 3D printing of porcelain by layerwise slurry deposition. *J. Eur. Ceram. Soc.* **2018**, *38*, 3395–3400. [CrossRef]

71. Erhard, P.; Angenoorth, J.; Reddersen, C.; Günther, D. Binder jetting at scale: Series production with sand and pathways to industrialization of slurry-based 3D printing. *Open Ceram.* **2026**, *25*, 2666–5395. [CrossRef]
72. Ruviaro, A.S.; Silvestro, L.; Santana, H.A.; Araújo, A.; Pelisser, F. Ternary sustainable geopolymer matrices containing metakaolin, water treatment sludge, and porcelain tile polishing residue. *Constr. Build. Mater.* **2024**, *440*, 137412. [CrossRef]
73. Industrial Sludge Management: Reducing Cost, Risk and Disposal Through Smart Thickening & Dewatering. Available online: https://watertecnik.com/blog/industrial-sludge-management-reducing-cost-risk-and-disposal-through-smart-thickening-dewatering-2/ (accessed on 13 August 2026).
74. Mizutani, R.F.; de Paula Santos, U.; Arbex, R.F.; Arbex, M.A.; Terra-Filho, M. An Evaluation of the Impact of Air Pollution on the Lung Functions of High School Students Living in a Ceramic Industrial Park Zone. *Int. J. Environ. Res. Public Health* **2023**, *20*, 6964. [CrossRef] [PubMed]
75. Xian, Z.; Zeng, L.; Cheng, X.; Wang, H. Effect of polishing waste additive on microstructure and foaming property of porcelain tile and kinetics of sinter-crystallization. *J. Therm. Anal. Calorim.* **2015**, *122*, 997–1004. [CrossRef]
76. Recycling Waste, Reusing Water, Reducing Consumption. The Italian Ceramic Tile Industry's Production Process Reuses All Waste Product and Wastewater. Available online: https://www.ceramica.info/en/articoli/recycling-waste-reusing-water-reducing-consumption/ (accessed on 13 August 2026).
77. Filter Press Applications in Ceramic, Tile, and Building Materials Wastewater Treatment. Available online: https://qdbritop.com/news/filter-press-ceramic-tile-building-materials-wastewater/ (accessed on 13 August 2026).

Disclaimer/Publisher's Note: The statements, opinions and data contained in all publications are solely those of the individual author(s) and contributor(s) and not of MDPI and/or the editor(s). MDPI and/or the editor(s) disclaim responsibility for any injury to people or property resulting from any ideas, methods, instructions or products referred to in the content.